

A Mass-Energy United Test of the Equivalence Principle

Mingsheng Zhan (✉ mszhan@wipm.ac.cn)

Wuhan Institute of Physics and Mathematics, APM, CAS <https://orcid.org/0000-0001-7240-1952>

Lin Zhou

Wuhan Institute of Physics and Mathematics, APM, CAS

Chuan He

Wuhan Institute of Physics and Mathematics, APM, CAS

Sitong Yan

Wuhan Institute of Physics and Mathematics, APM, CAS

Xi Chen

Wuhan Institute of Physics and Mathematics, APM, CAS

Dongfeng Gao

Wuhan Institute of Physics and Mathematics, APM, CAS

Weitao Duan

Wuhan Institute of Physics and Mathematics, APM, CAS

Yuhang Ji

Wuhan Institute of Physics and Mathematics, APM, CAS

Rundong Xu

Wuhan Institute of Physics and Mathematics, APM, CAS

Biao Tang

Wuhan Institute of Physics and Mathematics, APM, CAS

Chao Zhou

Wuhan Institute of Physics and Mathematics, APM, CAS

Sachin Barthwal

Wuhan Institute of Physics and Mathematics, APM, CAS

Qi Wang

Wuhan Institute of Physics and Mathematics, APM, CAS

Zhuo Hou

Wuhan Institute of Physics and Mathematics, APM, CAS

Zongyuan Xiong

Wuhan Institute of Physics and Mathematics, APM, CAS

Yuanzhong Zhang

Institute of Theoretical Physics, CAS

Min Liu

Chinese Academy of Sciences

Wei-Tou Ni

Wuhan Institute of Physics and Mathematics, APM, CAS

Jin Wang

Chinese Academy of Sciences <https://orcid.org/0000-0002-1830-8527>

Physical Sciences - Article

Keywords: Mass-Energy, Equivalence, energy

Posted Date: September 22nd, 2020

DOI: <https://doi.org/10.21203/rs.3.rs-63775/v1>

License:  This work is licensed under a Creative Commons Attribution 4.0 International License.

[Read Full License](#)

A mass-energy united test of the equivalence principle

Lin Zhou^{1,2,5}, Chuan He^{1,3,5}, Si-Tong Yan^{1,3}, Xi Chen^{1,2}, Dongfeng Gao^{1,2}, Weitao Duan^{1,3},
Yuhang Ji¹, Rundong Xu^{1,3}, Biao Tang^{1,2}, Chao Zhou¹, Sachin Barthwal¹, Qi Wang^{1,3},
Zhuo Hou^{1,3}, Zongyuan Xiong^{1,2}, Yuanzhong Zhang⁴, Min Liu^{1,2}, Wei-Tou Ni¹,
Jin Wang^{1,2,3*} & Mingsheng Zhan^{1,2,3*}

The equivalence principle (EP) is one of the basic assumptions of general relativity.

Almost all new theories¹ that attempt to unify gravity with the standard model²

require the EP be broken. Experimental tests of EP provide opportunities for

verification of different theoretical models and emergence of new physics.

Traditional mass tests³⁻⁹ of EP have achieved the precision of 10^{-15} level³. Tests with

quantum properties including spin^{10,11}, superposition¹², quantum statistics¹⁰ and

internal state^{4,13}, have been performed, and entanglement¹⁴ test was also proposed.

Energy is another very important property and is related to mass by the mass-energy

equivalence (MEE). However, mass-energy united tests of EP have never been

carried out. Here, we achieve for the first time the united EP test covering energy

interval from micro-eV to giga-eV by a mass and internal energy specified atom

interferometer (AI). The AI was realized by taking advantage of the Four-Wave

Double-diffraction Raman transition (4WDR) method⁷ for specified internal energy

states, and by extending 4WDR to include excited states. The Eötvös parameters of

the four paired combinations ($^{87}\text{Rb}|F=1\rangle$ - $^{85}\text{Rb}|F=2\rangle$, $^{87}\text{Rb}|F=2\rangle$ - $^{85}\text{Rb}|F=2\rangle$, $^{87}\text{Rb}|F$

$=1\rangle$ - $^{85}\text{Rb}|F=3\rangle$ and $^{87}\text{Rb}|F=2\rangle$ - $^{85}\text{Rb}|F=3\rangle$) were measured to be $\eta_1=(1.5 \pm 3.2) \times$

10^{-10} , $\eta_2=(-0.6 \pm 3.7) \times 10^{-10}$, $\eta_3=(-2.5 \pm 4.1) \times 10^{-10}$ and $\eta_4=(-2.7 \pm 3.6) \times 10^{-10}$,

¹ State Key Laboratory of Magnetic Resonance and Atomic and Molecular Physics, Wuhan Institute of Physics and mathematics, APM, Chinese Academy of Sciences-Wuhan National Laboratory for Optoelectronics, Wuhan 430071, China.

² Center for Cold Atom Physics, Chinese Academy of Sciences, Wuhan 430071, China.

³ School of Physical Sciences, University of Chinese Academy of Sciences, Beijing 100049, China.

⁴ Institute of Theoretical Physics, Chinese Academy of Sciences, Beijing 100190, China.

⁵ These authors contributed equally: Lin Zhou, Chuan He.

* e-mail: wangjin@wipm.ac.cn; mszhan@wipm.ac.cn

1 **respectively. The violation parameters of mass and internal energy are constrained to**
 2 **$\eta_0 = (-0.8 \pm 1.4) \times 10^{-10}$ and $\beta = (-0.6 \pm 6.9) \times 10^5$. This work opens a door for united**
 3 **tests of EP and MEE in large energy range with quantum systems.**

4
 5 Mass tests of EP have been performed in different ways including Lunar laser
 6 ranging¹⁵, torsion balance^{16,17}, satellite³ and AIs⁴⁻⁹. However, it is unknown whether the
 7 energy behaves the same as mass in a gravitational field although MEE holds at least at
 8 10^{-7} level¹⁸. To parameterize possible contributions of mass and energy to EP violation,
 9 under the condition that MEE is valid, we express the gravitational mass m_g of a test body
 10 as a sum of different types of mass-energy and their EP violation terms¹

$$\begin{aligned}
 m_g &= \sum_A (1 + \eta^A) \frac{E^A}{c^2} \\
 &= m_i + \sum_A \eta^A \frac{E^A}{c^2},
 \end{aligned}
 \tag{1}$$

11
 12 where $m_i \equiv \sum_A \frac{E^A}{c^2}$ is the inertial mass, A labels different interactions, E^A are their
 13 corresponding energies, c is the speed of light, and η^A are EP violation parameters. If EP
 14 validates, then $\eta^A = 0$. Up to now, EP tests using macro objects did not apparently involve
 15 energy. Only with microscopic particles as test bodies can it be possible to do energy
 16 dependent test of EP by selecting internal states of the particles. The early microscopic
 17 particle-based EP test was done by neutron interferometers^{19,20}. In recent years, with the
 18 development of atomic manipulation technology, Atom-based quantum test of EP has
 19 become possible. As listed in Table 1, mass tests with atoms have been performed using
 20 ^{85}Rb - ^{87}Rb , ^{87}Rb - ^{39}K and ^{88}Sr - ^{87}Sr atom pairs^{4,9,10}. Beyond-mass tests have been
 21 investigated using different quantum properties including quantum statistics¹⁰, spin^{11,12},
 22 superposition¹² and internal state^{4,13}. However, these experiments obtained either the mass
 23 violation coefficient or the energy violation coefficient. Up to now, no one has combined

1 mass and energy in one platform to precisely extract potential tiny difference between
2 mass and energy violation coefficients in noisy environments. The main obstacles lie in
3 the technical complexity when putting dual-species atoms and specific quantum states
4 together in AIs. It is rather difficult to satisfy the following requirements in one
5 experiment: (1) keeping the same specified quantum state in an AI; (2) suppressing
6 common mode noise for different species of atoms; (3) adjusting internal energy of atoms.
7 Here, we improve the 4WDR dual-species ^{87}Rb - ^{85}Rb AI⁷ and perform a united mass and
8 internal energy test of EP. Mass and internal energy specified AIs are realized by
9 deterministically manipulating the internal states of ^{87}Rb and ^{85}Rb atoms. Eötvös
10 parameters are measured for the four paired combinations, constraints to mass and energy
11 violation are then given respectively (see [Table 1](#)).

Table 1 | Measured Eötvös parameters of EP tests with atoms.

Mass Pair	$F-F'$	Mass Test	Beyond-Mass Test	Ref.
^{85}Rb - ^{87}Rb	2-1	$\eta = (1.2 \pm 1.7) \times 10^{-7}$	-	4
^{85}Rb - ^{87}Rb	mixed	$\eta = (1.2 \pm 3.2) \times 10^{-7}$	-	5
^{39}K - ^{87}Rb	mixed	$\eta = (0.3 \pm 5.4) \times 10^{-7}$	-	6
^{85}Rb - ^{87}Rb	2-1	$\eta = (2.8 \pm 3.0) \times 10^{-8}$	-	7
^{39}K - ^{87}Rb	mixed @ 0g	$\eta = (0.9 \pm 3.0) \times 10^{-4}$	-	8
^{39}K - ^{87}Rb	mixed	$\eta = (-1.9 \pm 3.2) \times 10^{-7}$	-	9
^{87}Sr - ^{88}Sr	9/2-0	$\eta = (0.2 \pm 1.6) \times 10^{-7}$	$k = (0.5 \pm 1.1) \times 10^{-7}$	10
^{85}Rb	2-3	-	$\eta = (0.4 \pm 1.2) \times 10^{-7}$	4
^{87}Rb	$m_F = \pm 1$	-	$\eta = (1.2 \pm 3.2) \times 10^{-7}$	11
^{87}Rb	1-2	-	$\eta = (1.4 \pm 2.8) \times 10^{-9}$	12
^{87}Rb	1-1 \oplus 2	-	$\eta = (3.3 \pm 2.9) \times 10^{-9}$	12
^{87}Rb	1-2	-	$\eta = (0.9 \pm 2.7) \times 10^{-10}$	13
Mass Pair	$F-F'$	Mass-Energy Test		
	1-2	$\eta_1 = (1.5 \pm 3.2) \times 10^{-10}$		
	2-2	$\eta_2 = (-0.6 \pm 3.7) \times 10^{-10}$		
^{87}Rb - ^{85}Rb	1-3	$\eta_3 = (-2.5 \pm 4.1) \times 10^{-10}$		This work
	2-3	$\eta_4 = (-2.7 \pm 3.6) \times 10^{-10}$		
		$\eta_0 = (-0.8 \pm 1.4) \times 10^{-10}$	$\beta = (-0.6 \pm 6.9) \times 10^5$	

13

14 In this experiment, we use ^{87}Rb and ^{85}Rb atom pairs with hyperfine levels, see Fig.1

15 (a). Then Eq. (1) is rewritten as ([Extra Data Eq.\(s1\)](#)),

$$\begin{cases} m_g^{87} = (1 + \alpha^{87}) m_i^{87} + \beta \frac{\Delta E^{87}}{c^2} \\ m_g^{85} = (1 + \alpha^{85}) m_i^{85} + \beta \frac{\Delta E^{85}}{c^2} \end{cases} \quad (2)$$

where α^{87} and α^{85} are the mass violation parameters of ^{87}Rb and ^{85}Rb atoms respectively, β is the internal energy violation parameter. ΔE is the internal energies (the difference of two hyperfine levels). The kinetic energy difference of atoms with a velocity of 2.5 m/s in the interference process is only less than 0.06 μeV . We assign different mass violation parameters to account for the different composition and complex interactions within each element. The EP violation between two test bodies is described by Eötvös parameter η ,

$$\eta \equiv \frac{\frac{m_g^{87}}{m_i^{87}} - \frac{m_g^{85}}{m_i^{85}}}{\frac{1}{2} \left(\frac{m_g^{87}}{m_i^{87}} + \frac{m_g^{85}}{m_i^{85}} \right)}. \quad (3)$$

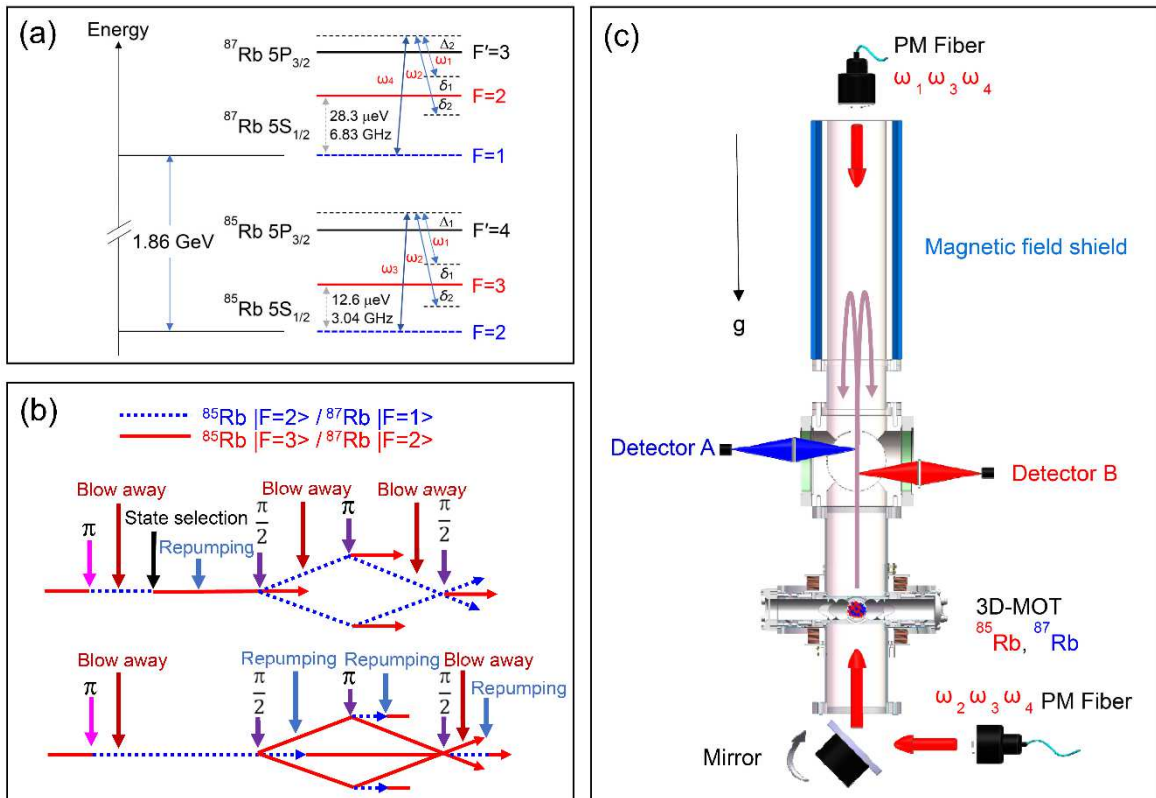
Inserting Eq. (2) into Eq. (3), taking the denominator approximately equal to 1, we get the Eötvös parameters of the four paired combinations as,

$$\eta_j = \eta_0 + \beta \chi_j, \quad (4)$$

where $\eta_0 \equiv \alpha^{87} - \alpha^{85}$, χ_j ($j=1, 2, 3, 4$) = (0, -1.6×10^{-16} , 3.5×10^{-16} , 1.9×10^{-16}) are scaled internal energy coefficients.

We proposed and implemented a 4WDR scheme (Fig. 1(a)) in our previous EP test⁷, the 4WDR dual-species AI owns advantages of symmetrical-recoil double-diffraction^{21,22}, common mode noise rejection and magic intensity ratio (MIR, it means the total ac Stark shift caused by Raman beams in dual-species Raman transitions is rejected to zero). However, the actual 4WDR AI needs to apply a blow away pulse to clear the remaining atoms in the middle path, as shown in the upper part of Fig. 1(b), which is not suitable for

1 preparing upper ground state (UGS) ($^{87}\text{Rb}|F=2\rangle$ or $^{85}\text{Rb}|F=3\rangle$) AI. To prepare UGS AI, as
 2 shown in the lower part of Fig. 1(b), an additional π -blow away pulse sequence is applied
 3 to prepare initial state and to select narrow velocity atoms, and a repumping pulse is added
 4 to make the intermediate path atoms deviate from the interference loop. At the end of
 5 interference, a blow away pulse is used to clear UGS atoms and a repumping pulse is used
 6 to pump atoms to UGS for high contrast detection. In addition, to ensure the
 7 synchronization of the dual-species atoms and reduce the systematic error, a π -blow
 8 away-state selection-repumping pulse sequences for the preparation of the initial state and
 9 speed selection are added to the lower ground state (LGS) ($^{87}\text{Rb}|F=1\rangle$ or $^{85}\text{Rb}|F=2\rangle$) AI, as
 10 shown in the upper part of Fig. 1(b). By doing this, the 4WDR is extended to be applicable
 11 to both LGS and UGS, which is called 4WDR-e scheme hereafter. In the experiment, the
 12 composition of the state selection pulses will be different for different atom pairs. The
 13 specific timing of the four combinations is detailed in Extra Data Fig.1.

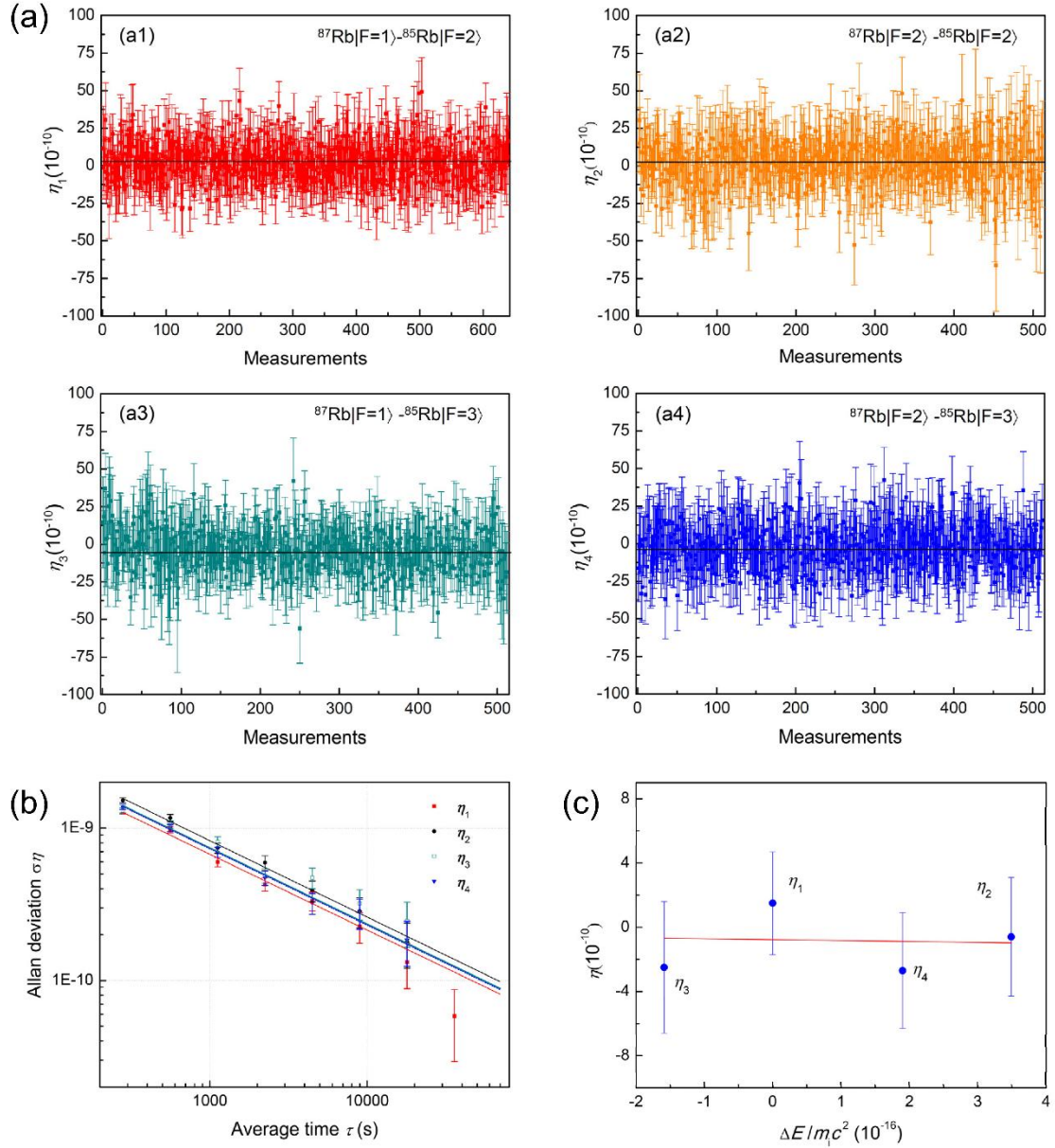


14

Fig. 1 | Schematic diagram of 4WDR-e ^{87}Rb - ^{85}Rb dual-species AI. (a) Relevant sub-levels covering energy interval from micro-eV to giga-eV. Raman lasers with frequencies of ω_1 , ω_2 , and ω_3 are used for ^{85}Rb atoms, while that with frequencies ω_1 , ω_2 , and ω_4 are for ^{87}Rb atoms; δ_1 is the detuning of ω_1 , δ_2 is the detuning of ω_2 . ω_1 and ω_2 are detuned to the blue side of transitions $^{85}\text{Rb}|F=3\rangle$ to $|F'=4\rangle$ with a detuning of Δ_1 and $^{87}\text{Rb}|F=2\rangle$ to $|F'=3\rangle$ with a detuning of Δ_2 . (b) The 4WDR-e configuration for ^{87}Rb - ^{85}Rb dual-species AI. The blue dash lines represent LGS atoms, and red solid lines represent UGS atoms. (c) Experimental setup. PM: polarization maintaining; 3D-MOT: three-dimensional magneto-optical trap.

The experimental setup is shown in Fig. 1(c), which it is upgraded from that in our previous work⁷. It is briefly described as follows. The three-dimensional magneto-optical trap (3D-MOT) of the lower part of the fountain is (0, 0, 1) configuration. The piezoelectric ceramic mounted mirror is for scanning the angle of the Raman lasers and compensating the Coriolis effect. A time-division-multiplexing method²³ is used to couple multiple laser beams in one fiber. A group of Raman beams (ω_1 , ω_3 , and ω_4) propagate downward through the top window of the vacuum chamber. Another group of Raman beams (ω_2 , ω_3 , and ω_4) propagate upward through the bottom window of the vacuum chamber. An active compensation is used to the magnetic field shield to further reduce fluctuation of the magnetic field. The fluorescence of ^{87}Rb and ^{85}Rb atoms is alternately collected by detector A and B to reduce errors caused by inconsistency of the detectors.

The statistical uncertainty is improved by improving atom numbers, compensating rotation of the Earth, increasing stability and free evolution time. To increase the signal to noise ratio and to suppress systematic errors, the z -direction effective temperature of the atoms participating in interference is lowered to 400 nK by selecting velocity group. The long-term system stability is improved by optimizing optics. The evolution time T among $\pi/2$ - π - $\pi/2$ Raman pulses is carefully adjusted to 203.164 ms to minimize ellipse-fitting error^{24,25}. The improvement footprint of Allan deviations of η measurements using $^{87}\text{Rb}|F=1\rangle$ - $^{85}\text{Rb}|F=2\rangle$ dual-species AI is shown in [Extended Data Fig. 2](#).



1

2 **Fig. 2 | Experimental data.** (a) Experimentally measured η values, where the error
 3 corresponding to the effective wave vector is corrected. (a1), (a2), (a3) and (a4) are
 4 measurements for η_1 , η_2 , η_2 and η_4 , respectively. (b) Allan deviation of η_1 (red
 5 squares), η_2 (black dots), η_3 (green boxes) and η_4 (blue triangles). (c) Dependence of
 6 η values on energy, the intercept value of the fitted straight line $\eta_0 = (-0.8 \pm 1.4) \times$
 7 10^{-10} , and the slope value $\beta = (-0.6 \pm 6.9) \times 10^5$.

8

9 The experimental data for four combination pairs are shown in Fig. 2. Fig. 2(a1)
 10 shows 640 measurements of η_1 value using $^{87}\text{Rb}|F=1\rangle\text{-}^{85}\text{Rb}|F=2\rangle$ atom pair, where each
 11 measurement is given by ellipse fitting (with free evolution time of 203.164 ms and

1 measurement time of 280 s for two detectors). The average value of these measurements is
2 2.5×10^{-10} . Fig. 2 (a2), (a3) and (a4) show 512 measurements of η_2 , η_3 and η_4 using
3 $^{87}\text{Rb}|F=2\rangle$ - $^{85}\text{Rb}|F=2\rangle$, $^{87}\text{Rb}|F=1\rangle$ - $^{85}\text{Rb}|F=3\rangle$ and $^{87}\text{Rb}|F=2\rangle$ - $^{85}\text{Rb}|F=3\rangle$ atom pairs,
4 respectively.

5 The Allan deviations are shown in Fig. 2(b). The red squares are data of η_1 , the
6 statistical uncertainty is 0.6×10^{-10} at an average time of 35840 s. The black dots, green
7 boxes, and blue triangles are data of η_2 , η_3 and η_4 , respectively. The corresponding
8 statistical uncertainties at an average time of 17920 s are 1.8×10^{-10} , 2.5×10^{-10} and $1.8 \times$
9 10^{-10} , respectively.

10 The systematic errors are suppressed by correcting the wave vector, optimizing MIR,
11 compensating the rotation of the Raman beams mirror, calibrating the gravity gradient
12 error, the quadratic Zeeman shift and suppressing the wave-front error.

13 The uncertainty of wave vectors is suppressed to 0.5×10^{-10} by precise frequency
14 control. The MIR is optimized from 1.0: 1.0: 3.1: 14 in our previous experiment⁷ to 1.00:
15 1.00: 3.05: 14.3 (Extra Data Fig.3). By improving the laser intensity control accuracy, the
16 ac Stark shift is evaluated by modulating the intensity of the Raman lasers, the final ac
17 Stark shift are evaluated as $\Delta\eta_1=(0.1 \pm 0.2) \times 10^{-10}$ (Extra Data Fig.4). The ac Stark shift
18 of other three combination pairs are evaluated as $\Delta\eta_2=(0.4 \pm 0.8) \times 10^{-10}$, $\Delta\eta_3=(0.0 \pm 0.2)$
19 $\times 10^{-10}$, $\Delta\eta_4=(-0.1 \pm 0.2) \times 10^{-10}$. The Coriolis error is suppressed by optimizing atom
20 cloud coincidence and compensating the rotation of the Raman beams mirror²⁴, the
21 Coriolis effect is suppressed²⁶ to -0.1×10^{-10} with an uncertainty of 0.4×10^{-10} . To
22 decrease the difference of positions and velocities of two atom clouds, the gravity gradient
23 phase shift is calibrated by adjusting the background magnetic field of the magneto-optical
24 trap (MOT), the laser frequency detuning of moving molasses. The phase shift caused by
25 position difference is 3.6×10^{-10} /mm (Extra Data Fig.5), the uncertainty corresponding

1 gravity gradient is calibrated as 2.8×10^{-10} by precise control of the position. The
 2 quadratic Zeeman shift is calibrated by modulating magnetic field. The magnetic field
 3 contribution to $^{87}\text{Rb}|F=1\rangle\text{-}^{85}\text{Rb}|F=2\rangle$ is $\Delta\eta_1 = (0.5 \pm 0.3) \times 10^{-10}$ (Extra Data Fig.6), and
 4 that for $^{87}\text{Rb}|F=2\rangle\text{-}^{85}\text{Rb}|F=3\rangle$, $^{87}\text{Rb}|F=2\rangle\text{-}^{85}\text{Rb}|F=2\rangle$, and $^{87}\text{Rb}|F=1\rangle\text{-}^{85}\text{Rb}|F=3\rangle$ are
 5 evaluated as $\Delta\eta_2 = (1.3 \pm 0.8) \times 10^{-10}$, $\Delta\eta_3 = (-1.3 \pm 0.8) \times 10^{-10}$, and $\Delta\eta_4 = (-0.5 \pm 0.3) \times$
 6 10^{-10} respectively.

7 The wave-front-aberration error is analyzed and estimated by modulating the size of
 8 detection beams. The error and uncertainty of the wave-front aberration analyzed from the
 9 actual experimental parameter is $(0.5 \pm 0.5) \times 10^{-10}$ (Extra Data Fig.7).

10 The contribution of other systematic error terms is evaluated less than 1.0×10^{-10} .

11 The final data of Eötvös parameters are shown in Fig. 2(c), fitting with Eq. (4) gives
 12 $\eta_0 = (-0.8 \pm 1.4) \times 10^{-10}$, $\beta = (-0.6 \pm 6.9) \times 10^5$. The error budget is summarized in Table 2.

13 **Table 2 Error budget**

Parameters	$\eta (\times 10^{-10})$				Uncertainty $\delta\eta (\times 10^{-10})$			
	η_1	η_2	η_3	η_4	$\delta\eta_1$	$\delta\eta_2$	$\delta\eta_3$	$\delta\eta_4$
Experimental data	49438.1	49437.5	49431.8	49432.7	0.6	1.8	2.5	1.8
Wave vector	49435.6	49436.0	49435.2	49435.6	0.5	0.5	0.5	0.5
ac Stark shift	0.1	0.4	0.0	-0.1	0.2	0.8	0.2	0.2
Coriolis effect	-0.1	-0.1	-0.1	-0.1	0.4	0.4	0.4	0.4
Gravity gradient	0.0	0.0	0.0	0.0	2.8	2.8	2.8	2.8
Quadratic Zeeman shift	0.5	1.3	-1.3	-0.5	0.3	0.8	0.8	0.3
Wave-front aberration	0.5	0.5	0.5	0.5	0.5	0.5	0.5	0.5
Others	0.0	0.0	0.0	0.0	1.0	1.0	1.0	1.0
Total	1.5	-0.6	-2.5	-2.7	3.2	3.7	4.1	3.6

14
 15 To conclude, we have completed a united test of EP using mass and internal energy
 16 specified atoms in one experiment. We observed no violation of EP at 10^{-10} level in
 17 $\mu\text{eV}\text{-GeV}$ mass-energy range. Compared with the previous tests, this work gives the mass
 18 constraint parameter η_0 and energy constraint parameter β simultaneously for the first time.
 19 This is also the first time to determine β . The current value of β was obtained from a large

1 mass-energy gap experiment, it can be further improved by other mass-energy
2 experiments such as metastable alkaline earth AI at eV region. Meanwhile, β in Eq.(4)
3 actually includes contribution of possible violation of MEE. With steady improvements of
4 AI technology, such as the application of high-sensitivity²⁷ and long-baseline²⁸, united and
5 even quantum tests^{29,30} of MEE and EP will become possible in the future.

7 **Online Content**

8 Methods, along with additional Extended Data display items and Source Data, are
9 available in the online version of the paper; references unique to these sections appear
10 only in the online paper.

- 11
12 1. Will, C. M. The confrontation between general relativity and experiment, *Living Rev.*
13 *Relativ.* **17**, 4(2014).
- 14 2. Safronova, M. S., Budker, D., DeMille, D., Kimball D. F. J., Derevianko, A. & Clark,
15 C. W. Search for new physics with atoms and molecules. *Rev. Mod. Phys.* **90**,
16 025008(2018).
- 17 3. Touboul P. *et al.*, MICROSCOPE Mission: first results of a space test of the
18 equivalence principle. *Phys. Rev. Lett.* **119**, 231101(2017).
- 19 4. Fray, S., Diez, C. A., Hänsch, T. W. & Weitz M. Atomic interferometer with
20 amplitude gratings of light and its applications to atom-based tests of the equivalence
21 principle. *Phys. Rev. Lett.* **93**, 240404(2004).
- 22 5. Bonnin, A., Zahzam. N., Bidel. Y. & Bresson. A. Simultaneous dual-species
23 matter-wave acceleromometer. *Phys. Rev. A* **88**, 043615(2013).
- 24 6. Schlippert, D., Hartwig. J., Albers. H., Richardson. L. L., Schubert, C., Roura, A.,
25 Schleich, W. P., Ertmer, W. & Rasel, E. M. Quantum test of the universality of free
26 fall. *Phys. Rev. Lett.* **112**, 203002(2014).

- 1 7. Zhou, L., Long, S. T., Tang, B., Chen, X., Gao, F., Peng, W. C., Duan, W. T., Zhong,
2 J. Q., Xiong, Z. Y., Wang, J., Zhang, Y. Z. & Zhan, M. S. Test of equivalence
3 principle at 10^{-8} level by a dual species double-diffraction Raman atom interferometer.
4 *Phys. Rev. Lett.* **115**, 013004(2015).
- 5 8. Barrett, B., Antoni-Micollier, L., Chichet, L., Battelier, B., Lévèque, T., Landragin, A.
6 & Bouyer, P. Dual matter-wave inertial sensors in weightlessness. *Nat. Commun.* **7**,
7 [13786\(2016\)](#)
- 8 9. Albers, H.,Herbst, A., Richardson, L. L., Heine, H., Nath, D., Hartwig, J.,
9 Schubert, C., Vogt, C., Woltmann, M.,Lämmerzahl, C., Herrmann, S., Ertmer, W.,
10 Rasel, E. M. & Schlippert, D. Quantum test of the universality of free fall using
11 rubidium and potassium. *Eur. Phys. J. D* **74**, 145 (2020).
- 12 10. Tarallo, M. G., Mazzoni, T., Poli, N., Sutyrin, D. V., Zhang, X. & Tino, G. M. Test of
13 Einstein equivalence principle for 0-spin and half-integer-spin atoms: search for
14 spin-gravity coupling effects. *Phys. Rev. Lett.* **113**, 023005(2014).
- 15 11. Duan, X. C., Zhou, M. K., Deng, X. B., Yao, H. B., Shao, C. G., Luo, J. & Hu, Z. K.
16 Test of the universality of free fall with atoms in different spin orientations. *Phys. Rev.*
17 *Lett.* **117**, 023001(2016).
- 18 12. Rosi, G., D’Amico, G., Cacciapuoti, L., Sorrentino, F., Prevedelli, M., Zych, M.,
19 Brukner, Č. & Tino, G. M. Quantum test of the equivalence principle for atoms in
20 coherent superposition of internal energy states. *Nat. Commun.* **8**, 15529(2017).
- 21 13. Zhang, K., Zhou, M. K. Cheng, Y., Chen, L. L., Luo, Q., Xu, W. J., Cao, L. S., Duan,
22 X. C., & Hu Z. K. Testing the universality of free fall by comparing the atoms in
23 different hyperfine states with Bragg diffraction. *Chin. Phys. Lett.* **37**, 043701(2020).
- 24 14. Geiger, R. & Trupke, M. Proposal for a quantum test of the weak equivalence
25 principle with entangled atomic species. *Phys. Rev. Lett.* **120**, 043602 (2018).

- 1 15. Hofmann, F. & Müller, J. Relativistic tests with Lunar laser ranging. *Class. Quantum*
2 *Grav.* **35**, 035015 (2018).
- 3 16. Hehl, F.W., von der Heyde, P., Kerlick, G. D. & Nester, J. M. General relativity with
4 spin and torsion: Foundations and prospects. *Rev. Mod. Phys.* **48**, 393 (1976).
- 5 17. Zhu, L., Liu, Q., Zhao, H. H., Gong, Q. L., Yang, S. Q., Luo, P. S., Shao, C. G., Wang,
6 Q. L., Tu, L. C. & Luo, J. Test of the equivalence principle with chiral masses using a
7 rotating torsion pendulum. *Phys. Rev. Lett.* **121**, 261101 (2018).
- 8 18. Rainville, S., Thompson, J. K., Myers, E. G., Brown, J. M., Dewey, M. S., Kessler Jr,
9 E. G., Deslattes, R. D., Börner, H. G., Jentschel, M. Mutti, P. & Pritchard, D. E. A
10 direct test of $E=mc^2$. *Nature* **438**, 1096–1097 (2005).
- 11 19. Koester, L. Verification of the equivalence of gravitational and inertial mass for the
12 neutron. *Phys. Rev. D* **14**, 907-909(1976).
- 13 20. Bertolami, O. & Nunes, F. M. Ultracold neutrons, quantum effects of gravity and the
14 weak equivalence principle. *Class. Quantum Grav.* **20**, L61-L66(2003).
- 15 21. Lévèque, T., Gauguet, A., Michaud, F., Pereira Dos Santos, F. & Landragin, A.
16 enhancing the area of a Raman atom interferometer using a versatile
17 double-diffraction technique. *Phys. Rev. Lett.* **103**, 080405 (2009).
- 18 22. Malossi, N., Bodart, Q., Merlet, S., Lévèque, T., Landragin, A. & Pereira Dos Santos,
19 F. Double diffraction in an atomic gravimeter. *Phys. Rev. A* **81**, 013617 (2010).
- 20 23. Yang, W., Zhou, L., Long, S. T., Peng, W. C., Wang, J. & Zhan, M. S.
21 Time-division-multiplexing laser seeded amplification in a tapered amplifier, *Chin.*
22 *Opt. Lett.* **13**, 012601(2015).
- 23 24. Foster, G. T., Fixler, J. B., McGuirk, J. M. & Kasevich, M. A. Method of phase
24 extraction between coupled atom interferometers using ellipse-specific fitting. *Opt.*
25 *Lett.* **27**, 951-953 (2002).

- 1 25. Wang, Y. P., Zhong, J. Q., Chen, X., Li, R. B., Li, D. W., Zhu, L., Song, H. W., Wang,
2 J. & Zhan, M. S. Extracting the differential phase in dual atom interferometers by
3 modulating magnetic fields. *Opt. Commun.* **375**, 34-37(2016).
- 4 26. Duan W. T., He C., Yan S. T., Ji Y. H., Zhou L., Chen X., Wang J., and Zhan M. S.,
5 Suppression of Coriolis error in weak equivalence principle test using ^{85}Rb - ^{87}Rb
6 dual-species atom interferometer. *Chin. Phys. B* **29**, 070305 (2020).
- 7 27. Asenbaum, P., Overstreet, C., Kim, M., Curti, J. & Kasevich M. A.
8 Atom-interferometric test of the equivalence principle at the 10^{-12} level.
9 [arXiv:2005.11624v1 \[physics.atom-ph\]](https://arxiv.org/abs/2005.11624v1) (2020).
- 10 28. Zhan, M. S. et al. ZAIGA: Zhaoshan long-baseline atom interferometer gravitation
11 antenna. *Intl. J. Mod. Phys. D* **29**, 1940005(2020).
- 12 29. Zych, M. & Brukner, Č. Quantum formulation of the Einstein equivalence principle.
13 *Nat. Phys.* **14**, 1027-1031 (2018).
- 14 30. Geiger, R. & Trupke M. Proposal for a quantum test of the weak equivalence principle
15 with entangled atomic species. *Phys. Rev. Lett.* **120**, 043602 (2018).

16

17 **Acknowledgments** We thank Shitong Long, Wendong Zhang and Jiaqi Zhong for their
18 contributions to the apparatus or key technology. This work was supported by National
19 Key Research and Development Program of China under Grant No. 2016YFA0302002,
20 National Natural Science Foundation of China under Grant Nos. 91536221, 91736311,
21 11574354 and 11204354, Strategic Priority Research Program of the Chinese Academy of
22 Sciences under grant Nos. XDB21010100, XDB23030100 and the Youth Innovation
23 Promotion Association of the Chinese Academy of Sciences under grant No. 2016300.

24 **Author Contributions** L.Z., J.W., and M.-S.Z. conceived the experiments. L.Z., C. H.
25 and S.-T.Y. carried out the experiment, J.W. and M.-S.Z. analyzed the data and wrote the

1 manuscript. W.-T.D., R.-D.X., Q.W., C.Z., Y.-H.J., S.B., Z.H., B.T. and Z.-Y.X.
2 contributed significantly to the early stages of the experiment. X.C., D.-F.G., M. L., Y.-Z.Z.
3 and W.-T.N. performed theoretical calculations. All authors read the manuscript. J.W. and
4 M.-S.Z. supervised the project.

5

6 **Author Information** Reprints and permissions information is available at
7 www.nature.com/reprints. The authors declare no competing financial interests. Readers
8 are welcome to comment on the online version of the paper. Correspondence and requests
9 for materials should be addressed to Jin Wang (wangjin@wipm.ac.cn) or Ming-Sheng
10 Zhan (mszhan@wipm.ac.cn).

11

1

2 **METHODS**

3 **EP formulation for rubidium atoms.** Following Eq.(1) and Fig. 1 (a), for rubidium
 4 atoms, the inertial mass is equal to the sum of the mass of lower ground state (LGS) and
 5 the internal mass-energy,

$$\begin{aligned}
 m_g &= (1 + \alpha) \frac{E^{\text{LGS}}}{c^2} + (1 + \beta) \frac{\Delta E}{c^2} \\
 &= m_i + \alpha m_0 + \beta \frac{\Delta E}{c^2} \\
 &\approx (1 + \alpha) m_i + \beta \frac{\Delta E}{c^2}
 \end{aligned} \tag{s1}$$

7 where $m_i \equiv \frac{E^{\text{LGS}}}{c^2} + \frac{\Delta E}{c^2}$ is the inertial mass, $m_0 \equiv \frac{E^{\text{LGS}}}{c^2}$ is the rest mass of LGS,

8 and $\Delta E \equiv E^{\text{UGS}} - E^{\text{LGS}}$ is the internal energy which is the difference between LGS and

9 UGS. $m_i \approx m_0$, because the internal energy ($\sim \mu\text{eV}$) is much smaller than the test mass

10 ($\sim \text{GeV}$). Eq. (4) is expanded as follows,

$$\left\{ \begin{array}{l} \eta_1 = \eta_0 \\ \eta_2 = \eta_0 - \beta \varepsilon^{85} \\ \eta_3 = \eta_0 + \beta \varepsilon^{87} \\ \eta_4 = \eta_0 + \beta (\varepsilon^{87} - \varepsilon^{85}) \end{array} \right. , \tag{s2}$$

12 where ε^{87} and ε^{85} are dimensionless energy scaling factors.

$$\varepsilon^{85} \equiv \frac{\Delta E^{85}}{m_{i0} c^2} = 1.6 \times 10^{-16} , \tag{s3}$$

$$\varepsilon^{87} \equiv \frac{\Delta E^{87}}{m_{i0} c^2} = 3.5 \times 10^{-16} . \tag{s4}$$

15 **The 4WDR-e atom interferometry.** As shown in Fig. 1(a), the frequencies of the Raman
 16 lasers satisfy the conditions:

$$\omega_1 + \delta_1 = \omega_2 - \delta_2 = \omega_3 - 3.04 \text{ GHz} = \omega_4 - 6.83 \text{ GHz}, \tag{s5}$$

1 where δ_1 and δ_2 ($\delta_1 = -\delta_2$) are two-photon detunings of ω_1 and ω_2 , respectively. The phase
 2 shift of dual-species AI is

$$3 \quad \Delta\phi = \Delta k_{\text{eff}} g (T + 2\tau) T (1 + 4\tau / \pi T), \quad (\text{s6})$$

4 where Δk_{eff} is the difference of effective wave vectors of the dual-species atoms, τ is the
 5 duration of the $\pi/2$ Raman pulses. As shown in Fig.3 (a) and (b) in Ref. [7], the ac Stark
 6 shift caused by Raman lasers can be eliminated by selecting the frequencies and
 7 optimizing the intensity ratio of the Raman lasers. The common-mode phase noise caused
 8 by shared ω_1 and ω_2 can be rejected. The phase noise of ω_3 and ω_4 are suppressed by
 9 double-diffraction Raman transition. The interference path in 4WDR AI is completely
 10 symmetrical, and the influence of the coupling between photon recoil and gravity gradient
 11 can be decreased to a large extent. In addition, the interference loop for one species atom
 12 keeps at the same internal state, thus the influence of different internal states is also
 13 reduced.

14 The 4WDR-e scheme is explained by taking ^{85}Rb atoms as an example.

15 For LGS AI, the π -blow away- π -repumping pulses are added for states preparation
 16 and velocity-selection. The atoms in the interference loop are kept in $|F=2\rangle$ state by
 17 performing upward and downward recoil operations on the atoms at the same time. During
 18 coherent operation, the atoms remaining in the $|F=3\rangle$ state will affect the interference.
 19 Therefore, a blow away pulse is added to clear atoms in $|F=3\rangle$ state.

20 For UGS AI, the π -blow away pulses are added for states preparation and
 21 velocity-selection. After the atoms interact with the first $\pi/2$ pulse, they are transited from
 22 $|F=2\rangle$ to $|F=3\rangle$. A repumping pulse is used to pump the atoms from $|F=2\rangle$ to $|F=3\rangle$.
 23 Although this process cannot completely clean up the atoms in $|F=2\rangle$ state, it can make
 24 them only as background without participating in the interference process. Due to the

1 presence of a repumping pulse, the atom number in the background increases sharply. In
2 order to decrease the background, we use a blow away-repumping pulse sequence after the
3 last Raman $\pi/2$ pulse, and only detect the atoms in $|F=2\rangle$ state which participate in the
4 interference loop. Note that, when the detected state is inconsistent with the interference
5 state, a π phase correction is required.

6 For dual-species AI with different atom pairs, atoms are initially prepared to states
7 $^{87}\text{Rb}|F=2\rangle$ and $^{85}\text{Rb}|F=3\rangle$. The additional pulse sequences can be arranged differently. The
8 specific pulse sequence for the four pairs is shown in [Extended Data Fig. 1](#). These pulse
9 sequences are described in detail as follows.

10 (a) $^{87}\text{Rb}|F=1\rangle$ - $^{85}\text{Rb}|F=2\rangle$ dual-species AI ([Extended Data Fig. 1\(a\)](#)). A π -blow
11 away- π -Repumping pulses sequence is applied to ^{87}Rb and ^{85}Rb for states preparation and
12 velocity-selection, after that atoms in states $^{87}\text{Rb}|F=2\rangle$ and $^{85}\text{Rb}|F=3\rangle$. Here, the π -pulse is
13 a weak single-diffraction Raman pulse, used to transfer narrow-velocity atoms. The blow
14 away pulse is used to clear the atoms residing in states $^{85}\text{Rb}|F=3\rangle$ and $^{87}\text{Rb}|F=2\rangle$, a
15 repumping pulse is applied for repumping atoms from $^{87}\text{Rb}|F=1\rangle$ and $^{85}\text{Rb}|F=2\rangle$ to
16 $^{87}\text{Rb}|F=2\rangle$ and $^{85}\text{Rb}|F=3\rangle$. A $\pi/2$ -blow away- π -blow away- $\pi/2$ pulses sequence is applied
17 to realize $^{87}\text{Rb}|F=1\rangle$ - $^{85}\text{Rb}|F=2\rangle$ dual-species AI. Here, the blow away pulse is used to clear
18 the $^{87}\text{Rb}|F=2\rangle$ and $^{85}\text{Rb}|F=3\rangle$ state atoms residing in the middle-path.

19 (b) $^{87}\text{Rb}|F=2\rangle$ - $^{85}\text{Rb}|F=2\rangle$ dual-species AI ([Extended Data Fig. 1\(b\)](#)). A π -blow away
20 pulses sequence is applied to ^{87}Rb atoms and a π -blow away- π_c -Repumping pulses
21 sequence is applied to ^{85}Rb atoms for states preparation and velocity-selection, after that
22 atoms in states $^{87}\text{Rb}|F=1\rangle$ and $^{85}\text{Rb}|F=3\rangle$. Here π_c -pulse is a co-propagating Raman pulse,
23 is used to transfer $^{85}\text{Rb}|F=2\rangle$ atoms to state $^{85}\text{Rb}|F=3\rangle$, the purpose of other laser pulses
24 are the same as those described in [Extended Data Fig. 1\(a\)](#). A $\pi/2$ -blow away- π -blow

1 away- $\pi/2$ pulses sequence is applied to realize $^{85}\text{Rb}|F=2\rangle$ AI and a
2 $\pi/2$ -repumping- π -repumping- $\pi/2$ pulses sequence is applied to realize $^{87}\text{Rb}|F=2\rangle$ AI. Here,
3 the repumping pulse is used to pumping atoms in states $^{87}\text{Rb}|F=1\rangle$ to $^{87}\text{Rb}|F=2\rangle$, the blow
4 away-repumping pulses sequence clear the atoms residing in states $^{87}\text{Rb}|F=2$ and pumping
5 atoms in states $^{87}\text{Rb}|F=1\rangle$ to $^{87}\text{Rb}|F=2\rangle$ for detection.

6 Since a co-propagating Raman pulse is used for state inversion of ^{85}Rb , ω_3 needs to
7 be reduced by 30 kHz after this pulse to compensate for the frequency shift caused by
8 photon recoil.

9 (c) $^{87}\text{Rb}|F=1\rangle$ - $^{85}\text{Rb}|F=3\rangle$ dual-species AI ([Extended Data Fig. 1\(c\)](#)). A π -blow
10 away- π -Repumping pulses sequence is applied to ^{87}Rb atoms and a π -blow
11 away- π_c -repumping- π -blow away pulses sequence is applied to ^{85}Rb atoms for states
12 preparation and velocity-selection. The purpose of laser pulses are the same as those
13 described in [Extended Data Fig. 1\(a\)](#) and [\(b\)](#). A $\pi/2$ -blow away- π -blow away- $\pi/2$ pulses
14 sequence is applied to realize $^{87}\text{Rb}|F=1\rangle$ AI, and a $\pi/2$ -repumping- π -repumping- $\pi/2$ pulses
15 sequence is applied to realize $^{85}\text{Rb}|F=3\rangle$ AI. The blow away-repumping pulses sequence
16 clear the atoms residing in states $^{85}\text{Rb}|F=3\rangle$ and pumping atoms in states $^{85}\text{Rb}|F=2\rangle$ to
17 $^{85}\text{Rb}|F=3\rangle$ for detection.

18 Since a co-propagating Raman pulse is used for state inversion of ^{85}Rb , ω_3 needs to
19 be increased by 30 kHz after this pulse to compensate for the frequency shift caused by
20 photon recoil.

21 (d) $^{87}\text{Rb}|F=2\rangle$ - $^{85}\text{Rb}|F=3\rangle$ dual-species AI ([Extended Data Fig. 1\(d\)](#)). A π -blow away
22 pulses sequence is applied to ^{87}Rb atoms and ^{85}Rb atoms for states preparation and
23 velocity-selection. The purpose of laser pulses are the same as those described in [Extended](#)
24 [Data Fig. 1\(a\)](#) and [\(b\)](#). A $\pi/2$ -repumping- π -repumping- $\pi/2$ pulses sequence is applied to

1 realize $^{87}\text{Rb}|F=2\rangle$ - $^{85}\text{Rb}|F=3\rangle$ dual-species AI. The blow away-repumping pulses sequence
 2 clear the atoms residing in states $^{87}\text{Rb}|F=2\rangle$ and $^{85}\text{Rb}|F=3\rangle$, and pumping atoms in states
 3 $^{87}\text{Rb}|F=1\rangle$, $^{85}\text{Rb}|F=2\rangle$ to $^{87}\text{Rb}|F=2\rangle$, $^{85}\text{Rb}|F=3\rangle$ for detection.

4 **Improvement of the signal to noise ratio.** To improve the signal-to-noise ratio of the
 5 atom fountain, we upgraded our original experimental setup³¹. We changed the 3D-MOT
 6 configuration from (0,1,1) to (0,0,1). A two-stage 2D-MOT was added to the 3D-MOT via
 7 a vacuum differential chamber. We also optimized laser wave-front and improved laser
 8 stability³². Allan deviations of η measurements using $^{87}\text{Rb}|F=1\rangle$ - $^{85}\text{Rb}|F=2\rangle$ dual-species AI
 9 are shown in [Extended Data Fig. 2](#), where (a) and (b) are the data for free evolution time T
 10 = 70.96 ms and $T=152.21$ ms before the setup upgrade. (c) is the data for $T=203.12$ ms
 11 after improvement of atom numbers and stability. (d) is the data for $T=203.44$ ms with
 12 rotation compensation, and (e) is the data for $T=203.164$ ms with all combined efforts.

13 **Assessment of systematic errors.** Systematic errors are calibrated by modulation
 14 experiments and theoretical calculation. These measures are described below.

15 (a) Correction of the wave vector. The phase shift difference between ^{85}Rb and ^{87}Rb
 16 atom interferometer is described as Eq. (s6). The values of Δk_{eff} with different atom pairs
 17 are listed in [Extended Data Table 1](#), where $T=203.164$ ms, $\tau=31$ μs , and the uncertainty of
 18 wave vector correction is 5×10^{-11} . The difference of Δf_{rec} value is caused by the frequency
 19 change of ω_3 after applying co-propagating state selection pulses.

20 **Extended Data Table 1 | The values of Δk_{eff} with different test pairs**

Test pairs	(1)	(2)	(3)	(4)
Δf_{rec} (kHz)	0	+30	-30	0
Δk_{eff} (m^{-1})	159.2402	159.2415	159.2390	159.2402
$\Delta \eta$ (10^{-10})	49435.6	49436.0	49435.2	49435.6

22 (1) $^{87}\text{Rb}|F=1\rangle$ - $^{85}\text{Rb}|F=2\rangle$

1 (2) $^{87}\text{Rb}|F=2\rangle$ - $^{85}\text{Rb}|F=2\rangle$

2 (3) $^{87}\text{Rb}|F=1\rangle$ - $^{85}\text{Rb}|F=3\rangle$

3 (4) $^{87}\text{Rb}|F=2\rangle$ - $^{85}\text{Rb}|F=3\rangle$

4
5 (b) ac Stark shift. The ac Stark shift is caused by Raman lasers, blow away and
6 repumping lasers. In our previous experiment⁷, the MIR of the Raman lasers was set to I_1 :
7 I_2 : I_3 : I_4 =1.0: 1.0: 3.1: 14 with an accuracy of 10%, which was limited by the fluctuation of
8 the Raman laser intensities. The maximum residual ac Stark shift was calibrated to be 6
9 kHz by modulating the Raman laser intensity from 10% to 100%. To reduce the shift, the
10 MIR of the four Raman lasers is controlled to I_1 : I_2 : I_3 : I_4 = 1.00: 1.00: 3.05: 14.3. The
11 long-term drift of the laser intensity is decreased to less than 2 % by controlling the
12 temperature of optics table, feedbacking, and isolation of the vibration of optics. The shift
13 is reduced to less than 500 Hz. The dependence of the ac Stark shift on the ratio precision
14 is shown in [Extra Data Fig. 3](#). To estimate the influence of the ac Stark shift on η , we
15 simulate the shift caused by Raman lasers as

$$\Delta\phi=8\tau(\varphi_{ac}^{dw}-\varphi_{ac}^{uw}), \quad (s7)$$

16
17 where φ_{ac}^{dw} and φ_{ac}^{uw} are ac Stark shifts of the downward part and the upward part of the
18 interference loop at the time of the second Raman pulse. This shift is mainly caused by the
19 residual ac Stark shift associated with the Raman laser intensity gradient. Considering
20 laser beams with a diameter of 30 mm, pulse duration $\tau = 30 \mu\text{s}$, evolution time $T = 203$
21 ms, and a residual ac Stark shift is less than 500 Hz, the calculated uncertainty of η caused
22 by ac Stark shift is less than 0.1×10^{-10} .

23 To investigate the ac Stark shift of blow away and Repumping lasers, we modulate
24 the duration of blow away pulses, and measure the $\Delta\eta_1$. The ac Stark shift contribution
25 due to blow away lasers is evaluated as 0.1×10^{-10} with the uncertainty of 0.2×10^{-10}
26 ([Extended Data Fig. 4](#)). According to [Extended Data Fig. 1\(b\), \(c\), and \(d\)](#), the blow away

1 and repumping lasers are different for specific combination pairs, the corresponding $\Delta\eta$
 2 values are $\Delta\eta_2 = (0.4 \pm 0.8) \times 10^{-10}$, $\Delta\eta_3 = (0.0 \pm 0.2) \times 10^{-10}$, $\Delta\eta_4 = (-0.1 \pm 0.2) \times 10^{-10}$.

3 (c) Coriolis effect. Due to the horizontal velocity distribution of atom clouds, the
 4 Coriolis effect caused by the Earth rotation couples to the free-falling atoms, so that the
 5 fluctuation of position and velocity of atom clouds leads to uncertainty of η measurement.
 6 The Coriolis effect is expressed as

$$7 \quad \Delta\phi = 2\mathbf{\Omega}_E \cdot (\Delta\mathbf{v}_0 \times \mathbf{k}_{\text{eff}}) T^2, \quad (\text{s8})$$

8 where $\mathbf{\Omega}_E$ is the Earth rotation, $\Delta\mathbf{v}_0$ is the velocity difference between two species atom
 9 clouds. Since the detectors are fixed, the phase difference mainly depends on the overlap
 10 degree of the atom clouds. In our experiments, the Coriolis effect is reduced mainly by
 11 two ways, one is to overlap the atom clouds and to reduce atom temperature; the other is
 12 to compensate the rotation of the Raman lasers mirror^{33,34}. We design and implement²⁶ a
 13 two-dimensional rotation compensation system for Raman lasers mirror. We perform
 14 rotation compensation for the east-west and the north-south direction. The phase responses
 15 to the rotation compensation are $\Delta\eta_{\text{E-W}} = 1.1 \times 10^{-9}/\Omega_E$ and $\Delta\eta_{\text{S-N}} = 1.6 \times 10^{-9}/\Omega_E$, the total
 16 residual contribution of the Coriolis effect is $\Delta\eta = (-0.1 \pm 0.4) \times 10^{-10}$.

17 (d) Gravity gradient. The phase shift caused by the position difference between the
 18 two atom clouds is³⁵ $\Delta\phi = k_{\text{eff}}\Delta g T^2$, where $\Delta g = T_{zz}\Delta h$, and T_{zz} is the gravity gradient in
 19 z -direction. The center positions of two atom clouds are measured by the time of flight
 20 (TOF) signal. The trajectory overlap of atom clouds is optimized by adjusting background
 21 magnetic field, detuning of moving molasses lasers, and velocity selection. We use three
 22 sets of pulses for gravity gradient modulation experiments. The first set of pulses is for
 23 velocity selection of ^{85}Rb and ^{87}Rb atom clouds. The second set of pulses makes ^{85}Rb and

1 ^{87}Rb clouds to obtain recoil velocities in opposite directions, so that their velocity
2 difference is $\Delta v=24$ mm/s. The third group of pulses reverses their velocity directions.
3 Thus, we modulate the relative position of two species atom clouds and measure gravity
4 gradient. The uncertainty of position difference measured in our experiments is 0.79 mm
5 which is mainly caused by time fluctuation of TOF signal. The corresponding gravity
6 difference is 3.6×10^{-10} g/mm, which is slightly larger than the typical value (3.1×10^{-10}
7 g/mm) on the surface of the Earth. The dependence of η measurements on the position
8 difference of two atom clouds is shown in [Extended Data Fig. 5](#). The uncertainty of η
9 measurement corresponding to gravity gradient is 2.8×10^{-10} .

10 The phase shift caused by the velocity difference between the two atoms clouds is
11 $\Delta\phi = k_{\text{eff}} T_{zz} \Delta v_0 T^3$. In our experiment, the velocity uncertainty due to the residual ac Stark
12 shift (<125 Hz), the quadratic Zeeman shift (<100 Hz), and the Raman laser frequency
13 difference (<100 Hz) is less than 100 $\mu\text{m/s}$. Considering $T_{zz} = 3.1 \times 10^{-7}$ g/m and $T =$
14 203.164 ms, the corresponding phase shift is 6×10^{-12} , which is much smaller than the
15 error of the gravity gradient term.

16 (e) Quadratic Zeeman shift. In ^{87}Rb - ^{85}Rb 4WDR dual-species AI, the phase shift due
17 to the quadratic Zeeman effect is given by

$$18 \quad \Delta\phi = 2\pi (Z_{87-F} - Z_{85-F}) \iint [B^{\text{uw}}(t)^2 - B^{\text{dw}}(t)^2] dt, \quad (\text{s9})$$

19 where I_c is the current of the C field coil, Z_{87-F} and Z_{85-F} are quadratic Zeeman shift
20 coefficients of ^{87}Rb and ^{85}Rb $|F, m_F=0\rangle$ states, B^{uw} and B^{dw} are magnetic fields of the
21 downward and upward path, respectively. The quadratic Zeeman shift of ^{85}Rb atoms was
22 measured by Li *et al.*³⁶. The Zeeman frequency shift coefficients of the magnetic sublevel
23 of ground fine structure of ^{87}Rb are $Z_{87-1} = -288$ Hz/G² (for $^{87}\text{Rb}|F=1, m_F=0\rangle$) and $Z_{87-2} =$
24 288 Hz/G² (for $^{87}\text{Rb}|F=2, m_F=0\rangle$), those of ^{87}Rb are $Z_{85-2} = -647$ Hz/G² (for $^{85}\text{Rb}|F=2,$
25 $m_F=0\rangle$) and $Z_{85-3} = 647$ Hz/G² (for $^{85}\text{Rb}|F=3, m_F=0\rangle$). The experimentally measured $\Delta\eta$

1 values for $^{87}\text{Rb}|F=1\rangle$ - $^{85}\text{Rb}|F=2\rangle$ with $I_c=50$ mA, 150 mA, 200 mA, and 300 mA are shown
 2 in [Extra data Fig. 6](#). The corresponding value of $\Delta\eta_i$ is fitted by

$$3 \quad \Delta\eta_i\kappa_i = aI_c^2 + bI_c + c, \quad (\text{s10})$$

4 where,

$$5 \quad \kappa_i = \frac{2k_{\text{eff}}gT^2}{2\pi(Z_{87-F}-Z_{85-F})} \quad (\text{s11})$$

6 for $\kappa_1(Z_{87-1}, Z_{85-2})$, we get $\Delta\eta_1 = (0.5 \pm 0.3) \times 10^{-10}$ when the I_c is extrapolated to 320 mA,
 7 where, the bias value (1.4×10^{-10}) of quadratic polynomial fitting includes the
 8 contributions of zero C-field and other experimental parameters. Since the contribution of
 9 the zero C-field (2×10^{-13}) can be ignored, the bias term is deduced from the contribution
 10 of quadratic Zeeman shift. According to Eq.(s10) and (s11), the corresponding $\Delta\eta$ values
 11 of the other three combination pairs given by using $\kappa_2(Z_{87-2}, Z_{85-2})$, $\kappa_3(Z_{87-1}, Z_{85-3})$, and
 12 $\kappa_4(Z_{87-2}, Z_{85-3})$ are evaluated as $\Delta\eta_2 = (1.3 \pm 0.8) \times 10^{-10}$, $\Delta\eta_3 = (-1.3 \pm 0.8) \times 10^{-10}$, and
 13 $\Delta\eta_4 = (-0.5 \pm 0.3) \times 10^{-10}$ respectively.

14 (f) Wave-front-aberration. We use the expansion-rate-selection method³⁷ to suppress
 15 the phase noise caused by the wave-front distortion of the Raman lasers. The
 16 corresponding error due to wave-front-aberration is analyzed and estimated by modulation
 17 experiments. We use the initial temperature of 3 μK , detection beam diameters of 5 mm,
 18 10 mm, 15 mm and 20 mm to measure the wave-front distortion. The experimentally
 19 measured $\Delta\eta$ value for $^{87}\text{Rb}|F=1\rangle$ - $^{85}\text{Rb}|F=2\rangle$ versus the size of detection beams is shown
 20 in [Extended Data Fig. 7](#). The actual beam diameter is 15 mm, so the contribution of
 21 wave-front distortion is fitted as $(0.5 \pm 0.5) \times 10^{-10}$.

22 (g) Other systematic errors. The errors caused by tides, absolute wavelength of lasers,
 23 chirp rate, mirror angle (pointing direction of the Raman beam), timing control accuracy

1 are suppressed in 4DWR-e AI and are small enough. The collision shift, which depends on
2 the density of the atoms, is also very small under present condition. The total uncertainty
3 of the contribution of these parameters is 1.0×10^{-10} .

4

5 31. Zhou, L., Xiong, Z. Y., Yang, W., Tang, B., Peng, W. C., Hao, K., Li, R. B., Liu, M.,
6 Wang, J. & Zhan, M. S. Development of an atom gravimeter and status of the
7 10-meter atom interferometer for precision gravity measurement, *Gen. Relativ. Gravit.*
8 [43, 1931 \(2011\)](#).

9 32. Zhou, C., Barthwal, S., Zhang, W. D., He, C., Tang, B., Zhou, L., Wang, J. & Zhan, M.
10 S. Characterization and optimization of a tapered amplifier by its spectra through a
11 long multi-pass rubidium absorption cell. *Appl. Opt.* [57, 7427-7434\(2018\)](#).

12 33. Louchet-Chauvet A., Farah T., Bodart Q., Clairon A., Landragin A., Merlet S. &
13 Pereira Dos Santos F. The influence of transverse motion within an atomic gravimeter.
14 *New J. Phys.* [13, 065025\(2011\)](#).

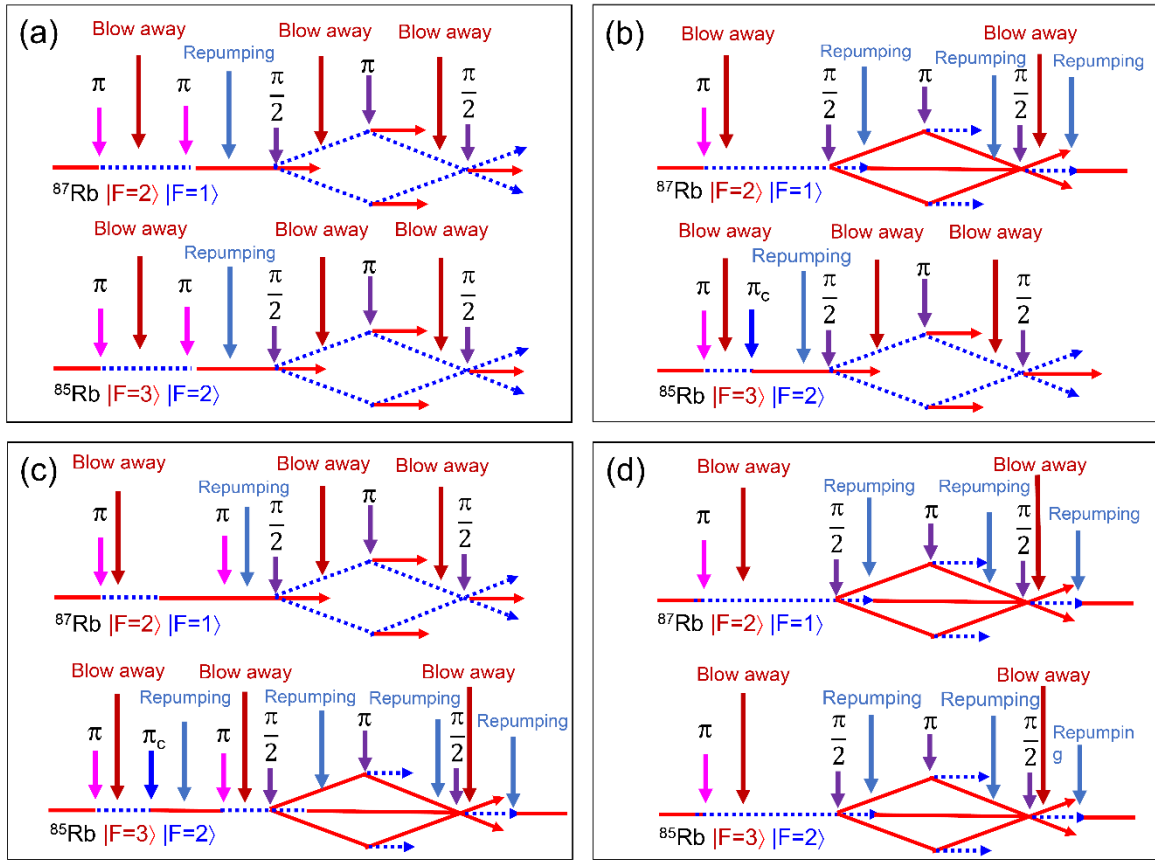
15 34. Lan, S. Y., Kuan, P. C., Estey, B., Haslinger, P. & Müller, H. Influence of the Coriolis
16 force in atom interferometry. *Phys. Rev. Lett.* [108, 090402\(2012\)](#).

17 35. Rothleitner Ch., & Svitlov S. On the evaluation of systematic effects in atom and
18 corner-cube absolute gravimeters. *Phys. Lett. A* [376,1090\(2012\)](#)

19 36. Li R. B., Zhou L., Wang J. & Zhan M. S. Measurement of the quadratic Zeeman shift
20 of ^{85}Rb hyperfine sublevels using stimulated Raman transitions. *Opt. Commun.* [282,](#)
21 [1340 \(2009\)](#).

22 37. Hu, J. G., Chen, X., Fang, J., Zhou, L., Zhong, J. Q., Wang, J. & Zhan, M. S. Analysis
23 and suppression of wave-front-aberration phase noise in weak-equivalence-principle
24 tests using dual-species atom interferometers. *Phys. Rev. A* [96, 023618\(2017\)](#).

1



2

3

4

5

6

7

8

9

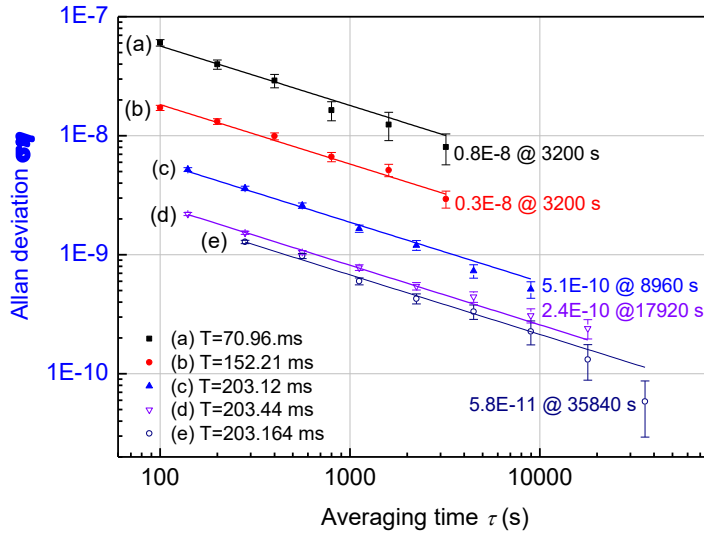
Extended Data Fig. 1 | Schematic diagram of mass and internal energy specified

4WDR dual-species AIs. (a) $^{87}\text{Rb}|F=1\rangle$ - $^{85}\text{Rb}|F=2\rangle$ dual-species AI. (b)

$^{87}\text{Rb}|F=2\rangle$ - $^{85}\text{Rb}|F=2\rangle$ dual-species AI. (c) $^{87}\text{Rb}|F=1\rangle$ - $^{85}\text{Rb}|F=3\rangle$ dual-species AI. (d)

$^{87}\text{Rb}|F=2\rangle$ - $^{85}\text{Rb}|F=3\rangle$ dual-species AI.

1



2

3

4

5

6

7

8

9

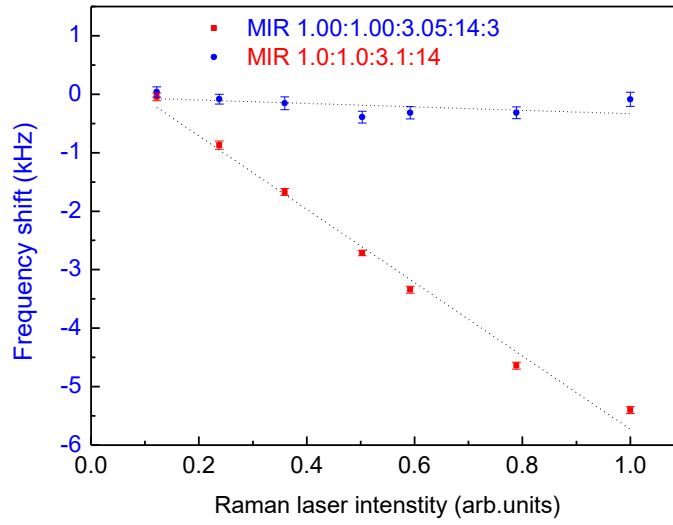
10

11

12

Extended Data Fig. 2 | Allan deviations of η measurements using $^{85}\text{Rb}|F=2\rangle$ - $^{87}\text{Rb}|F=1\rangle$ dual-species AI. (a) The statistical uncertainty of η is 8.0×10^{-9} at integral time of 3200 s and the free evolution time $T = 70.96$ ms. (b) The statistical uncertainty is improved to 3.0×10^{-9} with $T=152.21$ ms. (c) The statistical uncertainty is improved to 5.1×10^{-10} by the improvement of atom numbers, stability and $T=203.12$ ms. (d) The statistical uncertainty is improved to 2.4×10^{-10} by rotation compensation and $T=203.44$ ms. (e) The statistical uncertainty is improved to less than 5.8×10^{-11} by combined effort and $T=203.164$ ms.

1



2

3

4

5

6

7

8

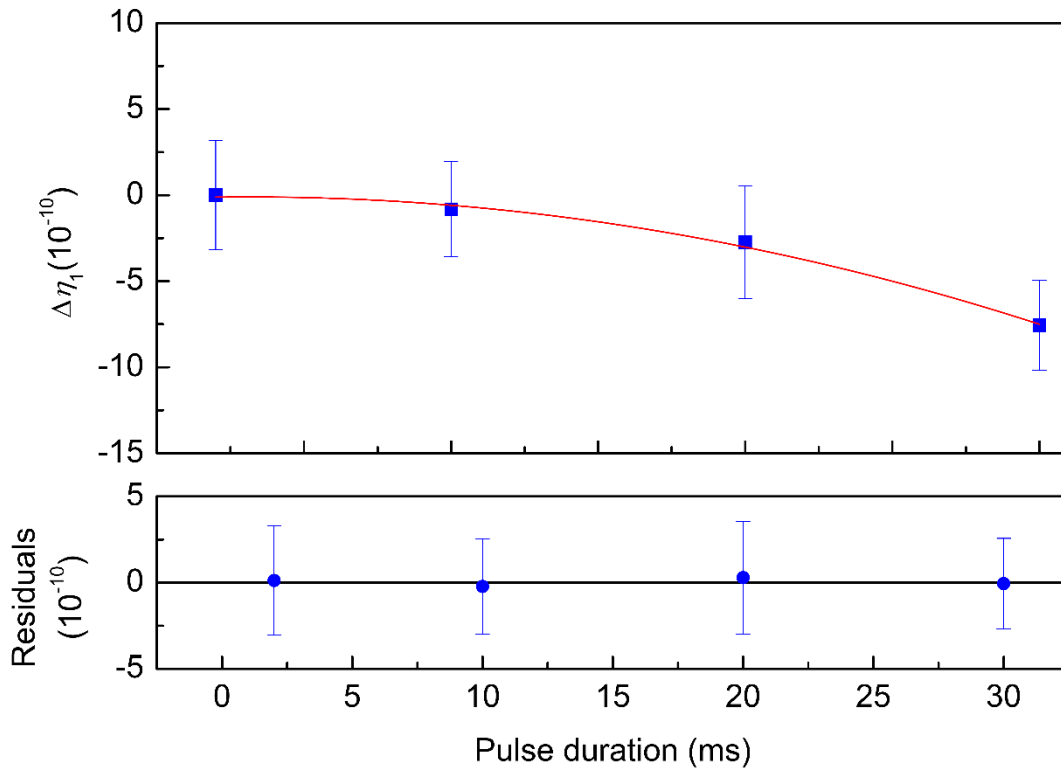
9

10

11

Extended Data Fig. 3 | Dependence of the ac Stark shift on the magic intensity ratio of the Raman lasers. MIR= $I_1: I_2: I_3: I_4$, which is magic intensity ratio of four Raman beams with frequencies of ω_1 , ω_2 , ω_3 , and ω_4 . The red dots are data before improvement when changing the Raman laser intensity from 10% to 100%, the maximum residual frequency shift is 6 kHz. The blue squares are data after improvement, and the frequency shift is less than 500 Hz. The error bars are obtained using Gaussian fitting.

1



2

3

4

Extended Data Fig. 4 | Dependence of η_1 measurements on the duration of blow away pulse. (a) The blue squares are experimental data, and the red curve is the quadratic polynomial fitting. The error bars are got by the Allan deviation with an integration time of 4480 s or 8960 s. The corresponding value of $\Delta\eta_1$ is fitted as 0.1×10^{-10} at pulse duration of 2 ms. (b) The residuals of quadratic polynomial fit, the uncertainty of $\Delta\eta_1$ is obtained as 0.2×10^{-10} by the deviation of residuals.

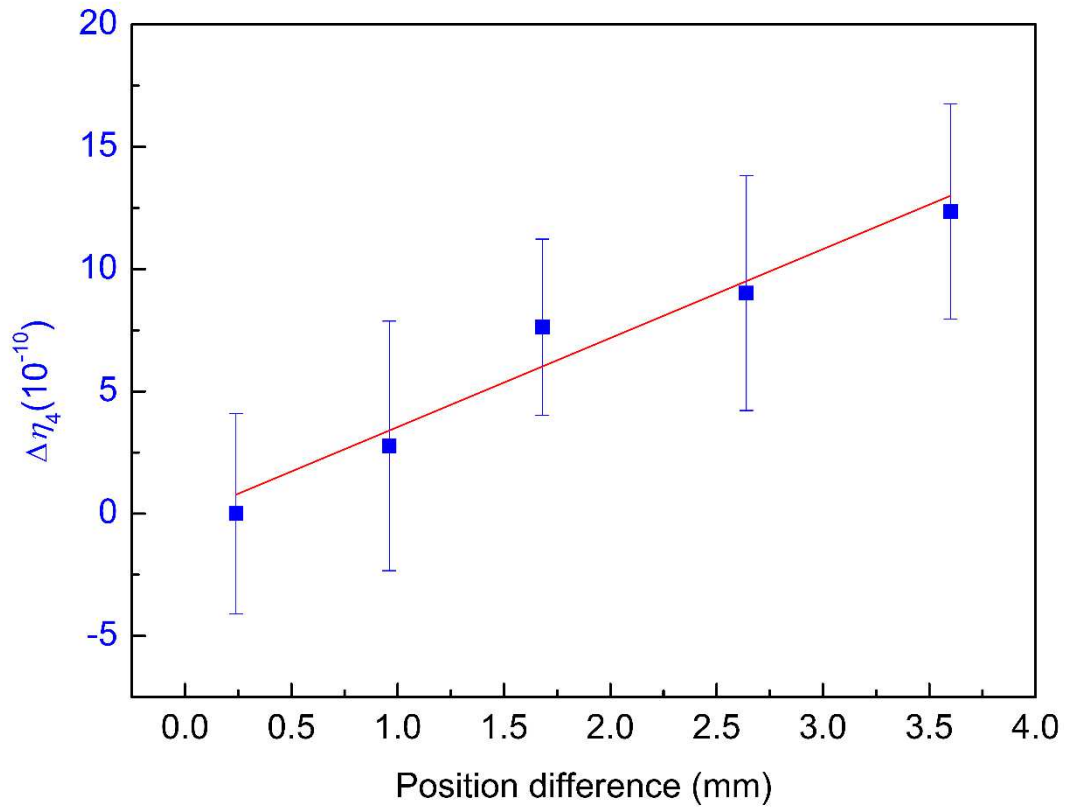
5

6

7

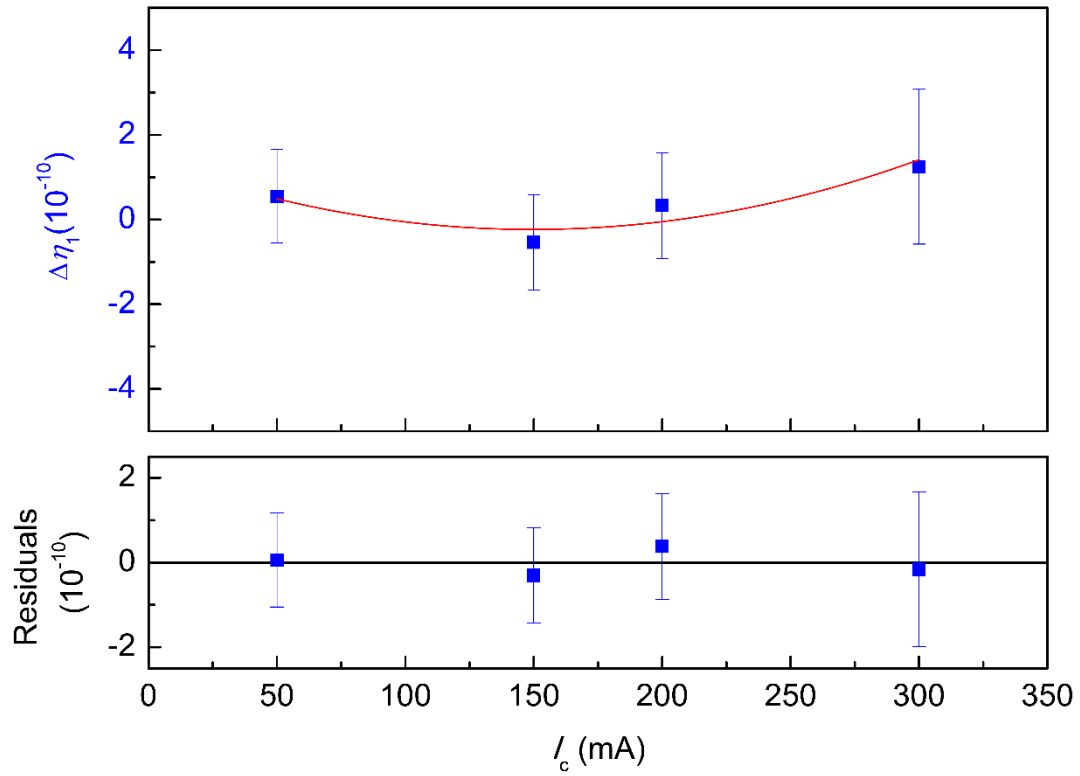
8

9



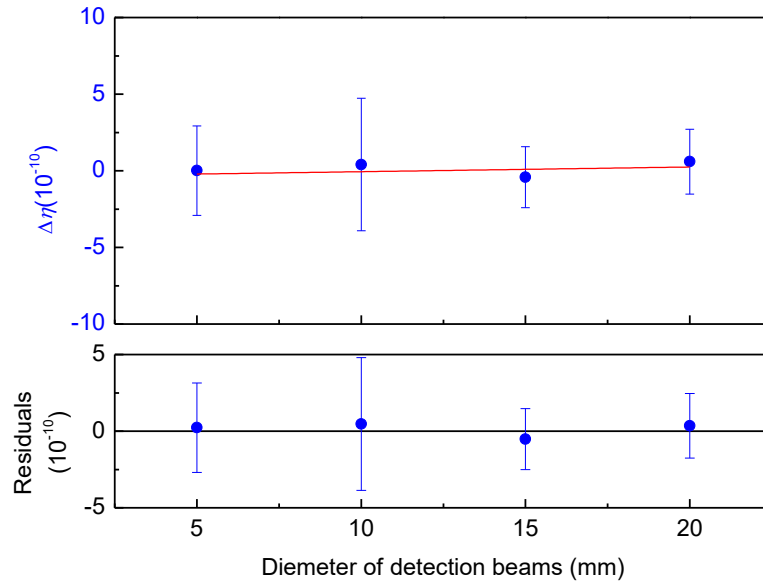
1
2
3
4
5
6
7
8

Extended Data Fig. 5 | Dependence of η_4 measurements on the position difference of two atom clouds. The velocity difference is 24 mm/s and the interval between velocity-selection pulses for ^{85}Rb and ^{87}Rb is 140 ms. The position difference is 3.36 mm, and the fitting value is $3.6 \times 10^{-10} / \text{mm}$. The error bars are got by the Allan deviation with an integration time of 4480 s or 8960 s.



1
2
3
4
5
6
7
8
9
10
11
12

Extended Data Fig. 6 | Dependence of uncertainty of η_1 measurements on the C-field current. (a) The blue squares are measurements using $I_C = 50$ mA, 150 mA, 200 mA, 300 mA. The error bars are got by the Allan deviation with an integration time of 4480 s or 8960 s. The black line is fitting curve. The corresponding value of $\Delta\eta_1$ is fitted as 0.5×10^{-10} when I_C is extrapolated to 320 mA. (b) The residuals of quadratic polynomial fit, the uncertainty of $\Delta\eta_1$ is obtained as 0.3×10^{-10} by the deviation of residuals.



1
2
3
4
5
6
7
8
9
10

Extended Data Fig. 7 | Dependence of η measurements on the size of detection beams. (a) The squares are measurements using detection beam with diameter of 5 mm, 10 mm, 15 mm, and 20 mm. The uncertainties of four measurements are all within 1.0×10^{-10} . The error bars are got by the Allan deviation with an integration time of 4480 s or 8960 s. The corresponding value of $\Delta\eta$ is fitted as 0.5×10^{-10} at beams diameter of 15 mm. (b) The residuals of quadratic polynomial fit, the uncertainty of $\Delta\eta$ is obtained as 0.5×10^{-10} by the deviation of residuals.

Figures

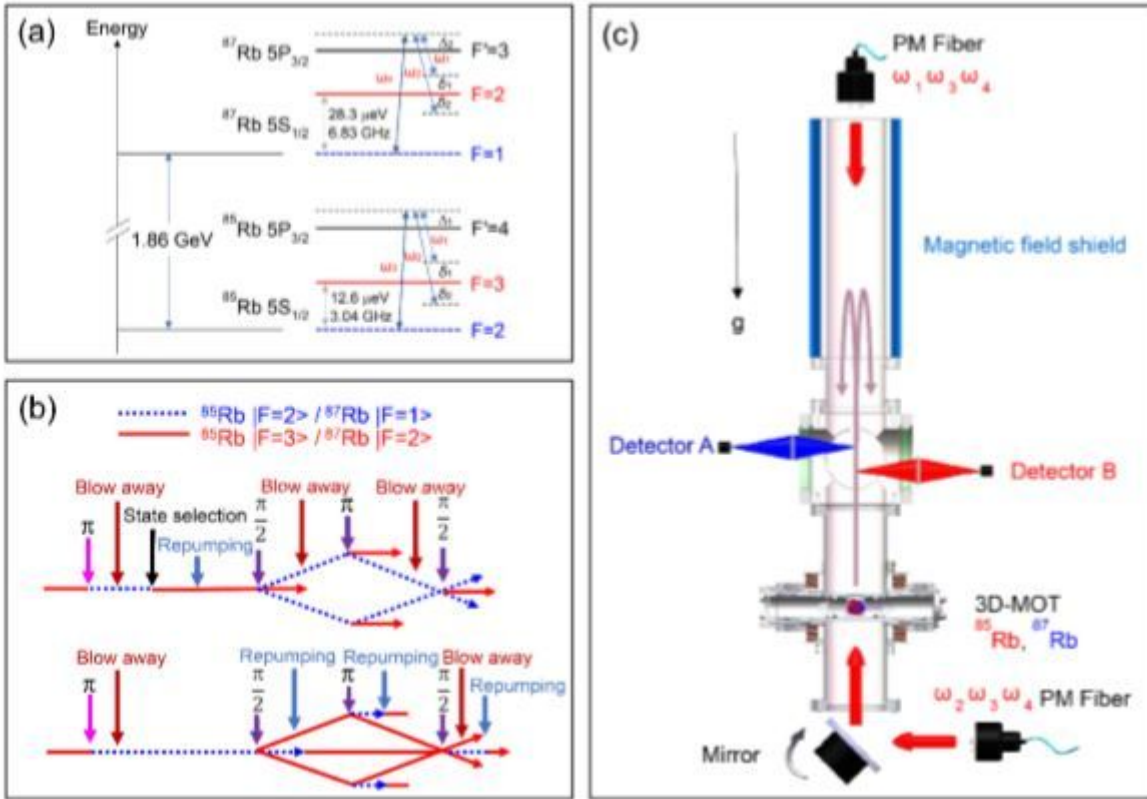


Figure 1

Schematic diagram of 4WDR-e ^{87}Rb - ^{85}Rb dual-species AI. (a) Relevant sub-levels covering energy interval from micro-eV to giga-eV. Raman lasers with frequencies of ω_1, ω_2 , and ω_3 are used for ^{85}Rb atoms, while that with frequencies ω_1, ω_2 , and ω_4 are for ^{87}Rb atoms; ω_1 is the detuning of ω_1 , δ_2 is the detuning of ω_2 . ω_1 and ω_2 are detuned to the blue side of transitions $^{85}\text{Rb} |F=3\rangle$ to $|F'=4\rangle$ with a detuning of Δ_1 and $^{87}\text{Rb} |F=2\rangle$ to $|F'=3\rangle$ with a detuning of Δ_2 . (b) The 4WDR-e configuration for ^{87}Rb - ^{85}Rb dual-species AI. The blue dash lines represent LGS atoms, and red solid lines represent UGS atoms. (c) Experimental setup. PM: polarization maintaining; 3D-MOT: three-dimensional magneto-optical trap.

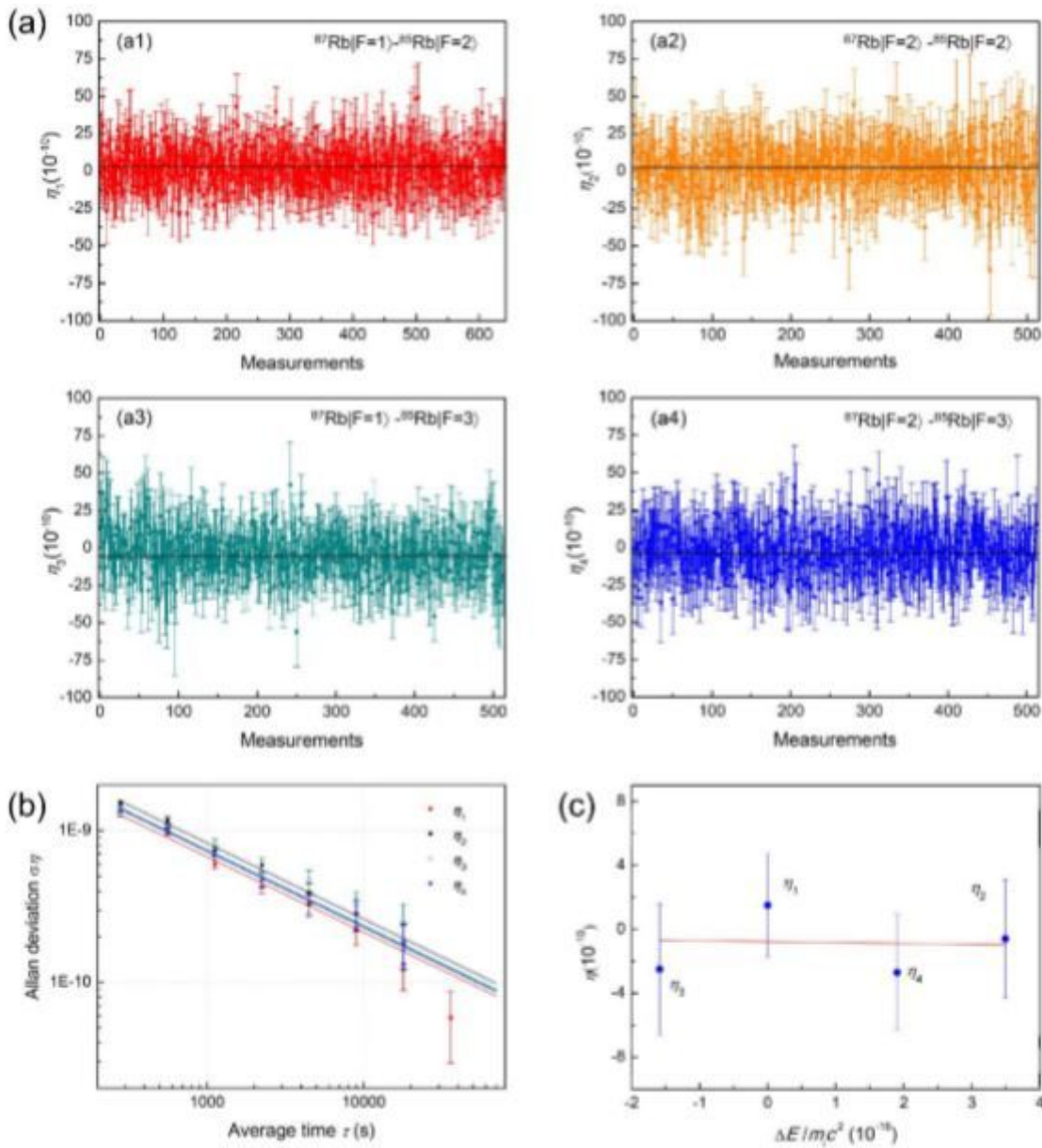


Figure 2

Experimental data. (a) Experimentally measured η values, where the error corresponding to the effective wave vector is corrected. (a1), (a2), (a3) and (a4) are measurements for η_1 , η_2 , η_2 and η_4 , respectively.

(b) Allan deviation of η_1 (red squares), η_2 (black dots), η_3 (green boxes) and η_4 (blue triangles). (c)

Dependence of η values on energy, the intercept value of the fitted straight line $\eta_0 = (-0.8 \pm 1.4) \times 10^{-10}$, and the slope value $\beta = (-0.6 \pm 6.9) \times 10^5$.